International Journal of Multiphase Flow 35 (2009) 603–616

Contents lists available at ScienceDirect

International Journal of Multiphase Flow

journal homepage: www.elsevier.com/locate/ijmulflow

A droplet transport model for channel and pipe flow based on particle kinetic theory and a stress–ω turbulence model

Roar Skartlien *

Institute for Energy Technology, P.O. Box 40, N-2027 Kjeller, Norway

ARTICLE INFO

Article history:
Received 16 July 2008
Received in revised form 17 February 2009
Accepted 12 March 2009
Available online 25 March 2009

Keywords:
Suspensions
Particle diffusivity
Turbophoresis
Particle continuum equations
Kinetic theory
Droplet transport

ABSTRACT

A model for droplet transport in turbulent gas–liquid flow in horizontal channels or pipes is developed. We invoke the kinetic theory of Reeks and co-workers for inertial particles, and the Reynolds stress-ω model of Wilcox for the gas turbulence. We introduce a suitable turbulence boundary condition at the gas–liquid interface. The full kinetic model is compared to experimental data using high density SF_6 gas and Exxsol oil, and the model gives a good prediction of the droplet distribution.

A simplified "first order model" that adopts a diameter-averaged eddy diffusivity from the full turbulence model, and that ignores the variation of the turbulence over the cross section, gives reasonable order of magnitude estimates of the droplet concentration profiles. There is, however, a clear tendency to overestimate the droplet concentration near the interface (and hence the axial droplet transport rate). Furthermore, the classical single phase pipe flow diffusivity ($0.075Ru^*$) underestimates the averaged eddy diffusivity by a factor of about two (giving too small concentration and transport rate).

The strength of the full kinetic model is that it correctly predicts a droplet diffusivity that accounts for the droplet inertia. This is important for the larger droplets close to the interface which contribute the most to the axial droplet transport rate. Hence, a simple eddy diffusivity will not correctly predict the droplet transport rate, since the droplet inertia is then ignored.

The droplet concentration in the upper half of the flow volume is dominated by the smaller droplets, and these are in contrast subject to the scalar eddy diffusivity. An elevated concentration close to the upper wall may be accounted for by a double-vortex secondary flow perpendicular to the axial mean flow.

1. Introduction

In pipelines or channels with stratified gas–liquid flow, frequently encountered in the nuclear and oil/gas industries, entrained droplets in the gas may constitute an important fraction of the total liquid flow rate. The goal in this paper is to construct a model for droplet transport accounting for variations in the gas turbulence level and stress in the flow cross section.

Previous work has shown that simple "first order modelling" of the droplet concentration in stratified liquid/gas flow, based on a particulate suspension in homogeneous turbulence, will not give fully satisfactory results when compared to experimental data (Skartlien, 2006). Such modelling consists of an exponential concentration profile for each droplet size, by assuming constant diffusivity (homogeneous turbulence) throughout the flow cross section. The data examined in this work were those of Tayebi et al. (2000), that covers the vertical diameter in a horizontal pipe.

First, the characteristic turbulent pipe flow diffusivity $0.075Ru^*$ (R is the pipe radius, or the half-height of the gas volume when the thickness of the liquid layer is appreciable) is too low to provide a sufficient scale height of the total concentration profile when the friction velocity u^* is estimated from standard pipe flow formulae from the given pressure drop. And second, the experimental concentration in the upper half of the flow volume shows a plateau, of even an increase with height, for moderate mean gas velocities. This could not be modelled by a superposition of simple exponential profiles with droplet-size dependent scale heights. For larger gas velocities where the concentration profile is less steep (with a flow cross section height smaller than 10 exponential scale heights), such a concentration plateau was not found.

The concentration in the lower half of the gas volume will influence the axial transport of fluid in the form of droplets, while the concentration of droplets in the upper half of the pipe is essential for the deposition of corrosion inhibitor and production chemicals on the pipe wall. Glycol based corrosion inhibitor is often injected in the water flowing in the bottom of the pipeline and the most likely mechanism for obtaining vertical transport of the corrosion inhibitor is turbulent diffusion of droplets.

* Tel.: +47 63 80 64 67; fax: +47 63 81 11 68.
E-mail address: roar.skartlien@ife.no

0301-9322/$ - see front matter © 2009 Elsevier Ltd. All rights reserved.
doi:10.1016/j.ijmultiphaseflow.2009.03.009

First order modelling captures only approximately the two most important effects – turbulent diffusion and gravity. Turbulent diffusion is providing the particle "lift", which is balanced by gravity. This type of rough diffusion model has been used by several authors (e.g., Paras and Karabelas, 1991) with reasonable success in flow of relatively large gas flow Reynolds numbers, even though some fundamental physical effects are ignored. The two most important (and well known) mechanisms that should be included is the effect of inhomogeneous turbulence, and the influence of particle inertia on the particle diffusivity. It is expected that inclusion of these effects will extend the applicability of the model.

Previous "higher order" Eulerian modelling efforts (e.g., Young and Leeming, 1997) have accounted for turbulence inhomogeneity, but a common ingredient has been coarse approximations of the particle diffusivity and turbophoretic drift induced by the gradient in turbulence kinetic energy. The current work attempts to improve this situation by invoking the kinetic theory of Reeks (1992) for particles (or droplets) in combination with a full Reynolds stress model for the gas. The kinetic theory automatically provides the needed generalized particle diffusivity to account for both small particles controlled by fluid diffusivity, and larger particles for which the fluid diffusivity plays no role (Skartlien, 2007).

In a general sense, the kinetic theory requires the full Reynolds stress tensor of the carrier phase. In simple channel flow geometry, only the wall normal stress is needed. In the current approach, the stress-ω model of Wilcox (2006) is implemented to accompany the kinetic theory. We will neglect two-way coupling between the droplets and the gas turbulence for now, even though particles or droplets in gas may dissipate or amplify the gas turbulence depending on the droplet size (e.g., Crowe, 2000; Drazen and Jensen, 2007).

For stratified air/water flow in horizontal pipes, Williams et al. (1996) found that the cross sectional droplet concentration may deviate from a horizontally stratified profile with monotonically decreasing concentration with height. This "deviatoric behavior" was also found in the data by Tayebi et al. (2000), as noted above, noting that the gas velocities were smaller and the gas density larger in the Tayebi data. To explain these anomalies in the droplet concentration profile, two hypotheses have been suggested by many authors: (1) Reynolds stress driven secondary flows in the pipe cross section generate sufficient cross sectional transport of droplets (Speziale, 1982, Williams et al., 1996), or (2) turbulence inhomogeneity modulates the distribution of droplets due to turbophoresis (Reeks, 1992). We will address both of these hypotheses in the current work.

In the following, we discuss the model equations and their boundary conditions, and compare the model results to experiments. The turbulence model is described in Section 2. A brief overview of the particle kinetic model is given in Section 3. Section 4 describes the calculation of concentration profiles. In Section 5 we compare the results to the experimental data of Tayebi et al. (2000). These experiments were done in a horizontal pipe of inner diameter of 9.95 cm containing Exxsol-D80 oil and dense SF_6 gas. The gas density and velocity represents field conditions. The discussion and conclusions are given in Section 6. Additional details are available in an Electronic annex available from the journal web page. These sections are referred to as the "annex" in the following text.

2. Wilcox' turbulence model modified for an interfacial boundary condition

We have adopted Wilcox' incompressible 1D channel flow code (Wilcox, 2006), solving for the full Reynolds stresses, the mean velocity, the turbulent kinetic energy k, and the specific dissipation rate ω, in the gas volume. The dissipation rate per unit of turbulent kinetic energy, is given by the relation $\epsilon = \beta^* k\omega$, where β^* is a constant. The Reynolds averaged momentum equation completes the model. We assume that the gas turbulence is unaffected by the droplets.

We have not attempted to construct a complete wall-to-wall turbulence model, including the interface. A model for the gas turbulence only, then implies that we need input parameters describing the interfacial stress and dissipation. We will tune these parameters such that the model predicts the correct velocity profile and eddy viscosity. We have modified the code of Wilcox (2006) to account for a fully turbulent interface (Biberg, 2005), while the treatment in the viscous sublayer near the wall is in its original form. We assume that the interface is fully turbulent, being controlled by the turbulence in either fluid. The viscous sublayer effect that would occur for a smooth or flat interface is then not included in the model.

The turbulence model is essentially a tri-diagonal matrix solver combined with iterations to solve the nonlinear set of equations. The matrices are conditioned to obtain the necessary stability in the iteration process. The turbulence model equations are solved through the viscous sublayer near the solid wall and down to the gas–liquid interface. The model equations are given in the annex. The model constants have been developed for single phase channel flow, and we adopt the same constants for the current application.

2.1. Considerations on channel flow geometry

The experimental work of Williams et al. (1996) demonstrates that the droplet concentration in the gas volume displays a strong influence of gravity for moderate gas velocities. In this regime, gravity and turbulent diffusion play an equally important role, and the cross sectional density contours in the pipe are roughly parallel to the gas/liquid interface. In this case one can justify the use of 1D models describing the cross sectional variation of the concentration profile along the vertical pipe diameter. We will therefore adopt a 1D modeling approach in this work, which will provide the concentration profile along the vertical diameter of the pipe.

The 1D model consists of a stratified, fully developed, statistically stationary droplet laden flow in a horizontal channel bounded by upper and lower walls that are parallel to the mean flow. Gravity acts in the vertical direction (y) perpendicular to the boundaries. For the fluid, we use $[u, v, w]$ for the fluctuating velocity components, and $[U, V, W]$ for the Reynolds averaged components, where the components refer to the streamwise (x), wall normal (y) and spanwise (z) components, respectively.

2.2. The momentum equation

For fully developed channel flow, the Reynolds averaged momentum equation is

$$-\partial_x P + \partial_y(\mu\partial_y U - \tau_{xy}) = 0, \tag{1}$$

where $\mu\partial_y U - \tau_{xy}$ is the total shear stress, $\tau_{xy} = \rho_g \overline{uv}$, $\mu = \rho_g \nu$ and the axial pressure gradient $\partial_x P$ is constant. Wilcox invokes the Boussinesq approximation at this stage relating the mean velocity to the Reynolds stress via the eddy viscosity,

$$\tau_{xy} = \rho_g \overline{uv} \simeq -\mu_T \partial_y U, \tag{2}$$

where $\mu_T = \rho_g \nu_T$. This gives the alternative equation in non-dimensional form (wall units)

$$(1 + \mu_T^+)\partial_{y^+} U^+ = 1 - (R+1)\frac{y}{h}. \tag{3}$$

One can relate the height y_m of maximum velocity ($\partial_y U = 0$), to $R = \tau_i/\tau_w$, via $1 - (R+1)y_m/h = 0$. Here, $\tau_w = \rho_g (u^*)^2$ is the wall

shear stress, and u^* is the wall friction velocity. We will adjust R so that the position of the modelled velocity maximum matches the measured maximum.

2.3. Input parameters to the turbulence model

The required parameters are the frictional Reynolds number $Re_\tau = hu^*/\nu$, shear stress ratio $R = \tau_i/\tau_w$, and the boundary value of the specific dissipation ω_i. In fact, h, R and ω_i would be output parameters from a complete wall-to-wall turbulence model that includes the interface.

The shear stress ratio R and ω_i are tuned to match the measured axial velocity profile $U(y)$. We adjust R so that the height y_m at which U is maximum, coincides with the measured height. The interfacial value ω_i is then adjusted to match the velocity profile near the interface. This latter tuning does not influence the velocity profile in the upper half of the flow volume very much.

The wall friction velocity is calculated from the given axial pressure gradient. For fully turbulent Poiseuille type channel flow of height h, the pressure gradient and the boundary shear stresses are related by

$$h|\partial_x P| = \tau_i + \tau_w, \tag{4}$$

when the shear stress variation over the thin viscous sublayer against the wall is ignored (recall that the total shear stress varies linearly). With the wall friction velocity $u^* \equiv \sqrt{\tau_w/\rho}$,

$$\frac{h|\partial_x P|}{\rho(u^*)^2} = R + 1. \tag{5}$$

For given h and axial pressure gradient $\partial_x P$, the wall friction velocity is given by

$$u^* = \sqrt{\frac{h|\partial_x P|}{(R+1)\rho}}. \tag{6}$$

We substitute h with the measured height of the gas volume at the vertical centerline. The interfacial friction velocity $u_i^* \equiv \sqrt{\tau_i/\rho}$ is then found by the relation

$$u_i^* = \sqrt{R}u^*. \tag{7}$$

This value is used for the characteristic velocity that controls the entrainment rate of droplets from the large scale interface. These entrainment relations are given in the annex (Binder and Hanratty, 1992; Guha, 1997; McCoy and Hanratty, 1977; Tatterson, 1975).

2.4. Interfacial boundary conditions for normal stress and k

Following Newton and Behnia (2001), the turbulent kinetic energy k_i at a fully turbulent interface is given in terms of interfacial shear stress $\tau_i = (\tau_{xy})_i$,

$$k_i = \frac{\tau_i}{\rho_g\sqrt{c_\mu}}, \tag{8}$$

where $c_\mu = 0.09$. Berthelsen and Ytrehus (2005) and Durbin et al. (2001) incorporate a roughness parameter R_s to account for the transition from a smooth to a rough surface,

$$k_i = \frac{\tau_i}{\rho_g\sqrt{c_\mu}}\alpha_k, \tag{9}$$

where

$$\alpha_k = \min[1, (R_s^+/90)^2]. \tag{10}$$

The roughness scale R_s^+ is given in wall units. For a fully turbulent interface defined by $R_s^+ > 90, \alpha_k = 1$. A specification of R_s^+ is then only necessary if the interface is not considered to be fully turbulent (e.g., via the RMS height of a wavy interface). In wall units,

$$k_i^+ = \frac{\rho_g k_i}{\tau_w} = R\left(\frac{\alpha_k}{\sqrt{c_\mu}}\right), \tag{11}$$

where $R = \tau_i/\tau_w$.

For the Reynolds stress equations that govern the deviatoric normal stresses, we find that Neumann interfacial boundary conditions are best suited. Here, the derivatives of $\sigma_i = \overline{u_i u_i} - 2/3k$ are set to zero,

$$\partial_y \sigma_i = 0 \tag{12}$$

such that the normal stress derivatives will be $(2/3)\partial_y k$. This approach ensures a smooth transition from the bulk flow to the interface. In contrast, setting fixed values at the interface (Dirichlet conditions) by the ad hoc assumption of isotropy in which the normal stresses are set to $2/3k$, yield large and possibly unrealistic gradients near the interface. However, the performance of the Neumann condition remains to be tested by comparison to experimental stress values. These are not available in the current data set.

Finally, we note that the interfacial boundary value of the specific dissipation is, in wall units,

$$\omega_i^+ = \frac{\alpha_k}{\beta_\omega \kappa\sqrt{c_\mu} Re_\tau}, \tag{13}$$

where κ is von Kármáns constant, and β_ω is a free parameter. The corresponding eddy viscosity is (Biberg, 2005)

$$(\nu_T^+)_i = \frac{k_i^+}{\omega_i^+} = Re_\tau \beta_\omega \kappa R. \tag{14}$$

Tuning ω_i via β_ω corresponds to an adjustment of the boundary eddy viscosity which in turn influences the velocity profile near the interface.

3. Reeks' particle kinetic model

We will adopt the kinetic theory of Reeks (1992) for a dilute particle suspension in turbulent gas flow. The current version of the theory is suitable for describing the transport properties of particles or droplets in a lighter surrounding fluid, with both light ($St \ll 1$) and heavy particles ($St \gg 1$) as defined by their Stokes number (St) in terms of the ratio between particle frictional relaxation time to turbulence integral timescale seen from the particles. Skartlien (2007b) finds that the correspondence is very good in both Stokes number regimes, confirming the general validity of the theory.

It is assumed (1) that the particle Reynolds number is sufficiently low such that only a linear drag-force in the particle equation of motion needs to be retained. In this case, one is able to separate the turbulent driving force on the particles from the friction force. For non-linear drag, separation can be obtained by performing a linearization procedure such that the drag coefficient becomes a function of the relative mean velocity between the particles and the fluid (e.g., Reeks, 1992). One also has to neglect lift forces due to *local vorticity* in the carrier fluid, but the lift contribution from the mean shear can be retained in the form of non-diagonal components of a drag tensor. Furthermore, (2) inter-particle collisions or interactions are neglected. These two assumptions are necessary to invoke the current form of the kinetic theory of Reeks. The basics of the theory are outlined in the annex.

3.1. Momentum and stress equations

In this section we will ignore the influence from secondary flows and set the mean fluid velocity and mean particle velocity in the cross section to zero. Later, we will discuss the effects of a secondary gas flow. For the fluctuating particle velocity compo-

nents we use the notation $[u_p, v_p, w_p]$, and $[U_p, V_p, W_p]$ for the ensemble averaged velocities. The components of the momentum equation as derived from kinetic theory become

$$\begin{aligned}
&\partial_y\left(\rho\overline{v_p v_p}\right) + \rho g_e = -\partial_y\left(\bar{\lambda}_{yy}\rho\right) - \bar{\gamma}_y\rho, \\
&\partial_y\left(\rho\overline{v_p u_p}\right) + \rho\beta(U_p - U) = -\partial_y\left(\bar{\lambda}_{yx}\rho\right) - \bar{\gamma}_x\rho, \\
&\partial_y\left(\rho\overline{v_p w_p}\right) = -\partial_y\left(\bar{\lambda}_{yz}\rho\right) - \bar{\gamma}_z\rho,
\end{aligned} \tag{15}$$

while the normal components of the stress equation become

$$\begin{aligned}
&\partial_y\left(\rho\overline{v_p v_p v_p}\right) + 2\beta\rho\overline{v_p v_p} = 2\rho\bar{\mu}_{yy}, \\
&\partial_y\left(\rho\overline{u_p u_p v_p}\right) + 2\beta\rho\overline{u_p u_p} = 2\rho\bar{\mu}_{xx} - 2\rho\mathscr{T}_{xy}\partial_y U_p, \\
&\partial_y\left(\rho\overline{w_p w_p v_p}\right) + 2\beta\rho\overline{w_p w_p} = 2\rho\bar{\mu}_{zz}.
\end{aligned} \tag{16}$$

The particle dispersion tensors $\bar{\lambda}$, $\bar{\mu}$ and $\bar{\gamma}$ all depend on the fluid Reynolds stresses, and in particular on the normal stress $\langle vv\rangle$ in the current channel flow setting (as we shall see below). The $\bar{\lambda}$ tensor introduces particle diffusion, $\bar{\mu}$ acts as a stress source, and $\bar{\gamma}$ induces a momentum source. The axial stress equation has an additional source due to the mean shear $\partial_y U_p$. For further information on the kinetic theory, see the annex and Hyland et al. (1999), Swailes et al. (1998) and Reeks (2001, 2005).

3.2. Particle dispersion coefficients

The dispersion coefficients can be written (e.g., Reeks, 1992),

$$\bar{\lambda}_{yy} = \langle v_p f_y'\rangle, \tag{17}$$

$$\bar{\mu}_{yy} = \langle v_p f_y'\rangle, \tag{18}$$

where the wall normal force is $f_y' = v/\tau_p$. To evaluate these coefficients, we invoke Green's function of the EOM to express the position y_p and velocity v_p in terms of f_y'. This results in the evaluation of the auto-correlation function

$$C_{yy}(\mathbf{x}, \mathbf{x}_p) = \langle f_y'(\mathbf{x}, t) f_y'(\mathbf{x}_p(s), s)\rangle, \tag{19}$$

where $\mathbf{x}_p(s)$ is the particle position $[x_p, y_p, z_p]$ at time $s \leqslant t$, and $\mathbf{x} = \mathbf{x}_p(t)$ is a chosen evaluation point in the medium, through which the particle passes at time t. Thus, the ensemble average (over all turbulence realizations) is referred to a fixed evaluation point $\mathbf{x}$ and a stochastic point $\mathbf{x}_p(s)$.

We now apply the locally homogeneous approximation. This means that we treat the turbulence (f_y') as if it were homogeneous, but at the local values. Such an approximation gives reasonable results for a wide range of Stokes numbers (Skartlien, 2007). In homogeneous turbulence, the following essential simplification can be made: *The two-point force correlations can be expressed in terms of a time dependent exponential decay of the local single-point correlations* (e.g., Reeks, 1992). This gives

$$C_{yy} \simeq \langle f_y'(\mathbf{x}, t) f_y'(\mathbf{x}, t)\rangle \exp\left\{\frac{-(t-s)}{\tau}\right\}, \tag{20}$$

where the characteristic correlation time is τ. The dispersion components are now given by the explicit form

$$\bar{\lambda}_{yy} = \langle vv\rangle \frac{(\tau/\tau_p)^2}{1 + \tau/\tau_p}, \tag{21}$$

$$\bar{\mu}_{yy} = \frac{\bar{\lambda}_{yy}}{\tau}, \tag{22}$$

where $\langle vv\rangle$ is the wall normal stress of the carrier fluid. For stationary flow, the Reynolds time average $\overline{vv}$ is equivalent to the ensemble average,

$$\overline{vv} = \langle vv\rangle \quad \text{for stationary flow}, \tag{23}$$

such that the Reynolds averages from the turbulence model can be used as to calculate the dispersion tensor components above.

We further adopt the "passive scalar approximation – PSA" (Skartlien, 2007) for the dispersion vector component $\bar{\gamma}_y$,

$$\bar{\gamma}_y = -\partial_y\left(\bar{\lambda}_{yy}\right). \tag{24}$$

This approximation assures the correct behavior for the momentum equation in incompressible flow in the limit of small particle Stokes number.

3.3. Turbulence correlation time seen from particles

One can show that the wall normal particle diffusivity limits to

$$(\epsilon_{yy})_h = \langle vv\rangle\tau, \tag{25}$$

when transport of kinetic stress can be ignored, and when the locally homogeneous form of the dispersion tensor $\bar{\lambda}_{yy}$ is invoked. This limit is then appropriate for the smaller particles where the eddy diffusivity is the relevant diffusivity. If we assume a Schmidt number of unity, the eddy diffusivity is equal to the eddy viscosity (i.e., the momentum diffusivity). Consistency between the eddy diffusivity and the particle diffusivity for vanishing relaxation time (passive tracer particles adjust to the flow instantaneously), then implies the following correlation time

$$\tau = \nu_T/\langle vv\rangle. \tag{26}$$

3.4. Concentration profile and particle diffusivity

With given dispersion tensor component $\bar{\lambda}_{yy}$, drift coefficient $\bar{\gamma}_y$, and normal stress $\overline{v_p v_p}$, the formal solution of (15) in terms of particle density (or concentration) is

$$\rho(y) = \rho(0)\frac{\epsilon_{yy}(0)}{\epsilon_{yy}(y)} \exp\left\{-\tau_p \int_0^y \frac{g_e + \bar{\gamma}_y(\zeta)}{\epsilon_{yy}(\zeta)}\, d\zeta\right\}, \tag{27}$$

where ϵ_{yy} is the wall normal component of the particle diffusivity tensor.

The particle diffusivity follows directly from the basic assumptions of (1) a simplified EOM with (2) a Gaussian turbulence force. The diffusivity has two contributions: a wall normal stress contribution $\tau_p\overline{v_p v_p}$ and a contribution due to the direct forcing by the carrier fluid turbulence, $\tau_p\bar{\lambda}_{yy}$,

$$\epsilon_{yy}(y) = \tau_p\left(\overline{v_p v_p} + \bar{\lambda}_{yy}\right). \tag{28}$$

Both contributions are mainly controlled by the fluid normal stress $\langle vv\rangle$ in the current channel flow setting (with $\overline{v_p v_p}$ driven by $\bar{\mu}_{yy}$). The normal stress contribution $\tau_p(\overline{v_p v_p})$ dominates for the larger Stokes numbers, while for smaller Stokes numbers, the term $\tau_p\bar{\lambda}_{yy}$ dominates. In the limit of vanishing relaxation time, $\tau_p\bar{\lambda}_{yy}$ converges to the passive scalar diffusivity. It is then clear that a particle diffusivity approximation based on a passive scalar diffusivity only will fail for larger Stokes numbers. In most previous modelling efforts, however, the particle diffusivity is usually set equal to the eddy viscosity of the fluid (which is equal to the passive scalar diffusivity for a Schmidt number of unity). One would assume that this is a potentially valid approximation for low Stokes numbers (small droplets).[1]

For the special case of homogeneous turbulence, ϵ_{yy} reduces to a constant and $\bar{\gamma}_y = 0$, such that an exponential profile is recovered,

$$\rho(y) = \rho(0)\exp\left\{-\frac{\tau_p g_e}{\epsilon_{yy}} y\right\}.$$

[1] Skartlien (2007) evaluates $\bar{\lambda}_{yy}$ directly from particle tracking simulations, and finds that the eddy viscosity of the fluid is only a coarse approximation to the particle diffusivity, even for the low Stokes number regime. This reflects the well known fact that a diffusivity defined in terms of a gradient diffusion flux is generally a non-local quantity in inhomogeneous media (inhomogeneous turbulence) through the path-history of the particles.

Although widely used as a first approximation, we note that the exponential profile is not strictly applicable in wall bounded flow, where turbulence is always inhomogeneous. We will see in the following that accounting for inhomogeneous turbulence can give significant improvements compared to a homogeneous approximation. This approach involves the simultaneous solution of the momentum equation (15) and stress equation (16), which is relatively straightforward.

3.5. Boundary conditions, numerical solution and input parameters

The density (or concentration) boundary condition $\rho(0)$ for the concentration profile (27) may be determined from the empirical entrainment and deposition relations as described in the annex. The relaxation time is $\tau_p = V_T/g$ which we define in terms of the terminal velocity V_T and the acceleration of gravity, g. The terminal velocity is calculated according to the annex (Rivkind and Ryskin, 1976). The turbulence normal stress $\langle vv\rangle$ and timescale τ is provided from the Reynolds stress model.

In order to close the stress equation (16), we apply the Chapman–Enskog relation (e.g., Sergeev et al., 2002; Zaichik and Alichenkov, 2005),

$$\overline{v_p v_p v_p} \simeq -\epsilon_{yy}\partial_y \overline{v_p v_p}. \tag{29}$$

This closure relation for the triple correlation truncates the formally infinite set of equations to second order. Combining (15) and (16) with the Chapman–Enskog relation, gives a *single equation* for $\overline{v_p v_p}$, in the form of the non-linear second order equation

$$\beta^2 \overline{v_p v_p} + \left(\frac{g_e + \bar{\gamma}_y}{2}\right)\partial_y \overline{v_p v_p} - \left(\frac{\epsilon_{yy}}{2\tau_p}\right)\partial_y^2 \overline{v_p v_p} = \beta \bar{\mu}_{yy}. \tag{30}$$

The two required boundary conditions may be chosen as the endpoint values of the normal stress (Dirichlet conditions). We have not considered Neumann conditions yet. A solution can be obtained by linearization and Newton–Raphson iteration. The linearized differential equation corresponds to a tri-diagonal matrix equation which is easy to implement numerically.

The stress boundary conditions are defined by adopting the local form of the stress equation, which will result if the transport of kinetic stress is set to zero,

$$2\beta\rho\overline{v_p v_p} = 2\rho\overline{\mu_{yy}}. \tag{31}$$

This translates to

$$\overline{v_p v_p} = \tau_p \overline{\mu_{yy}} = \langle vv\rangle \frac{\tau/\tau_p}{1+\tau/\tau_p}. \tag{32}$$

This relation provides a reasonable limiting behavior; for large Stokes number (heavy particles) the boundary kinetic stress will be much smaller than the fluid stress, and for vanishing Stokes number, the particle stress will be equal to the fluid stress. The last assumption is accurate while the former assumption may be questionable. We find that for the larger droplets, a moderate amplification of the estimated stress provides a better match to the experimental concentration profile near the interface. We will therefore use the form

$$\overline{v_p v_p} = \langle vv\rangle \frac{\tau/\tau_p}{1+\tau/\tau_p} f(\tau/\tau_p), \tag{33}$$

where the "amplification factor"

$$f(\tau/\tau_p) = 1 + \frac{a}{1+\tau/\tau_p} \tag{34}$$

is designed such that $f \to 1$ for small droplets and $f \to 1+a$ for heavier droplets. To obtain a reasonable match to the data for all cases, we found that $a = 1/2$ gave good results. This gives a factor 3/2 larger value of the normal stress for heavy droplets ($\tau/\tau_p \to 0$). For the upper boundary, we set $f = 1$ since only the smaller droplets will be present here.

4. Calculation of the total concentration profile

4.1. Integration over the size distribution

The turbulence model equations are solved first, and the output is then given as input to the kinetic model for the droplets. The particle equations are solved for each droplet size, and the full concentration profile is obtained by integration over the size bins. This approach is valid when coalescence, breakup and turbulence modification in the bulk flow can be ignored.

The total density profile is obtained by summing over all the density bins,

$$\rho(y) = \sum_i \rho_i(0) c_i(y), \tag{35}$$

where $c_i(y)$ is the concentration profile normalized to the value at $y = 0$. These concentration profiles (for droplets with diameter d_i) are obtained from the kinetic theory with the turbulence model input. The corresponding boundary densities $\rho_i(0)$ are determined from the Rosin–Rammler distribution, and the total boundary density. See annex for the determination of droplet diameters, relaxation time and boundary density, respectively.

4.2. First order modelling

We will compare the concentration profiles to those generated by first order modelling. For first order modelling, each size bin is associated with their own scale height H_i giving a profile $\rho_i(y) = \rho_i(0)\exp(-y/H_i)$. The total density profile is now

$$\rho(y) = \sum_i \rho_i(0)\exp(-y/H_i). \tag{36}$$

The scale height for bin i is

$$H_i = \frac{\epsilon}{(V_T)_i} \tag{37}$$

and $(V_T)_i$ is the terminal velocity of the droplet with diameter d_i (Ueda, 1979; Yoon, 2005, see annex). Here, ϵ is a characteristic diffusivity that is assumed to be independent of droplet size,

$$\epsilon = \zeta(h/2)u^*_{\text{eff}}, \tag{38}$$

where $\zeta = 0.075$ is the non-dimensional scalar diffusivity in the core regions of single phase pipe flow. This estimate may be reasonable for the smaller droplets that follow the fluid closely, but not for the larger droplets due to inertial effects that give appreciable velocity differences between the fluid and the droplets.

To match the characteristic diffusivity in the current in two-phase flow, we define an effective friction velocity u^*_{eff}. The first choice is the average between wall and interface values,

$$u^*_{\text{eff}} = (u^*_i + u^*)/2. \tag{39}$$

A more representative approach for wall-interface configurations is to simply adopt the average value of the eddy viscosity from the Wilcox model,

$$\hat{\epsilon} = \frac{1}{h}\int_0^h \nu_T(y)\,dy \equiv \zeta(h/2)\hat{u}^*_{\text{eff}}. \tag{40}$$

We will test both of these estimates below.

5. Comparison to pipe flow experiments

5.1. Flow parameters

The experiments were carried out using an iso-kinetic probe, as described in detail by Tayebi et al. (2000). We use four test cases

Table 1
Flow parameters. The superficial and maximum gas velocities are given together with the pressure gradient (pressure drop), gas density and mean interface height relative to the pipe floor. The RMS wave height at the interface is σ_y. The inner pipe diameter is 9.95 cm.

Case	U_{sg} (m/s)	U_{max} (m/s)	$\partial_x P$ (Pa/m)	ρ_g (kg/m^3)	y_i (mm)	σ_y (mm)
A	4.33	5.68	88	23.4	27.0	4.0
B	4.51	5.64	117	32.5	26.0	4.5
C	6.89	8.17	192	23.4	21.5	4.5
D	7.00	8.01	240	32.5	18.5	3.0

Table 2
Wall friction velocities, Reynolds numbers and core values $\tau_m = \max(\tau)$ of the turbulence timescale.

Case	u^* (m/s)	Re_τ	Re	τ_m (ms)
A	0.30	33,400	628,000	38
B	0.31	49,500	905,000	42
C	0.49	59,300	995,000	27
D	0.49	86,000	1,408,000	29

taken from the Tayebi data. Cases A and B are the low velocity cases, while cases C and D are the high velocity cases. The gas densities were set to a high and a low value for each value of the superficial gas velocities. Table 1 summarizes the flow parameters.

The gas volume height is $h = D_i - y_i$ where the inner pipe diameter is $D_i = 99.5$mm, and y_i is the liquid thickness (or interface height) along the vertical diameter. The viscosity of the SF_6 gas is $\mu = 1.5 \times 10^{-5}$; Ns/m^2 and for the Exxsol oil, $\mu_d = 1.6 \times 10^{-3}$ Ns/m^2. The surface tension between the oil and gas is $\sigma = 22 \times 10^{-3}$ N/m. The oil density is 820 kg/m^3. The gas Reynolds number $Re = hU_{max}/\nu$ and the friction Reynolds number Re_τ are given in Table 2, together with the wall friction velocities.

The tuned parameters are given in Table 3. These are the droplet mean diameter, relative to the Azzopardi (1985)-formula (see annex), the relative standard deviation of the Rosin–Rammler size distribution, the fitted shear stress ratio R, and the fitted β_ω parameter that controls the specific dissipation at the interface (which again controls the eddy viscosity at the interface). Recall that R and β_ω is needed as input or tuning parameters in the current gas turbulence model. In principle, these parameters could be taken as output from a complete wall-to-wall turbulence model including the gas–liquid interface.

Table 3
Tuned parameters. a is the amplification on the lower boundary kinetic stress relative to the homogeneous value, $\bar{d}/d_{32}$ is the calibration factor on the Azzopardi mean droplet size formula (see annex). $\sigma_d/\bar{d}$ is the normalized width of the Rosin–Rammler size distribution. R is the shear stress ratio based on the location of the maximum of the mean velocity profile. β_ω is the interfacial eddy viscosity calibration factor, adjusted to match the mean velocity near the interface.

Case	a	$\bar{d}/d_{32}$	$\sigma_d/\bar{d}$	R	β_ω
A	1.5	1.5	0.7	1.9	0.050
B	1.5	1.5	0.7	1.8	0.050
C	1.5	2.0	0.7	1.7	0.035
D	1.5	2.0	0.7	1.5	0.035

5.2. Turbulence profiles and timescales

The gas turbulent kinetic energy, stress components and timescale τ for case A (Re = 628,000) is given in Fig. 1. The turbulent

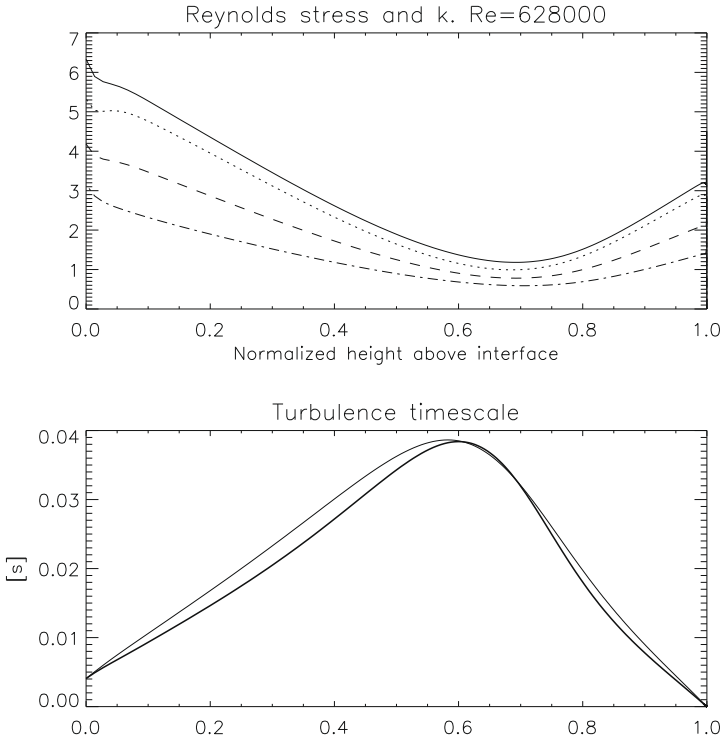

Fig. 1. Case A (Re = 628,000). Top: turbulent kinetic energy k (solid line), axial stress $\overline{uu}$ (dotted), spanwise stress $\overline{ww}$ (dashed) and wall normal stress $\overline{vv}$ (dash-dot). The profiles are normalized to $(u^*)^2$. Bottom: the thin line shows the adopted timescale $v_T/\overline{vv}$ which is consistent with scalar diffusivity, and the thick line $\tau = 2/\omega$.

kinetic energy reaches a minimum in the core flow near 0.65 flow volume heights. The normal stress $\overline{vv}$ (dash dotted line) is about one half the kinetic energy k (full line). The profile shapes are not very sensitive to the Reynolds number, although they are somewhat flatter for the larger Reynolds number, with smaller interface values relative to $(u^*)^2$. Only in the very narrow wall region will the profile shapes differ significantly with Reynolds number, but this is not visible in the full-range plot. The turbulence timescale τ reaches a maximum where the turbulence energy is a minimum, and the timescale diminishes towards the wall and the interface where the characteristic eddy sizes and turnover times are smaller.

5.3. Concentration and mean velocity profiles

Figs. 2–5 show the results for all cases, without invoking secondary flow. The upper left panel shows the density data (crosses) together with the density from the kinetic model (thin full line). The dash-dotted lines are the first order model profiles resulting from using a single characteristic eddy diffusivity. The thin dash-dotted line is the result from using the diffusivity (38), and the thick dash-dotted line is the result from using the cross sectional average of the eddy viscosity (40).

The lower right panels show the eddy viscosity as the thin full line (normalized to $[h/2]u^*$). The thin horizontal line shows the classical pipe core value $\zeta = 0.075$, and the thin dotted line shows the diffusivity (38) with the average friction velocity. The thick dotted line shows the cross sectional average (40). We note that this value is about twice the value of (38). Thus, for a first order model to give reasonable concentration profiles, we require a cross sectionally averaged diffusivity, rather than the estimate (38), or the classical pipe core value.

The first order model (with cross sectionally averaged eddy diffusivity) matches the data well for cases A and B, except in upper parts of the flow volume, where the data shows an *increasing* concentration with height towards the pipe roof. This behavior is not possible to encapsulate with first order modelling. Kinetic modelling does a slightly better job, with somewhat elevated concentration in the upper parts, but the increasing density is not captured. We will address this by invoking secondary flow later.

The situation is different for cases C and D for higher gas velocity. The largest deviation between the first order model and the data are now found near the interface. Here, the density profile in the data is steeper than the first order profile. This indicates that the average eddy diffusivity overpredicts the actual diffusivity close to the interface. The kinetic model (thin full line) seems to predict profiles with a qualitative match to the data.

Near the interface, only heavy inertial droplets with the larger Stokes numbers contribute significantly to the concentration. The diffusivity for these droplets is controlled by the kinetic stress. Nonlocal coupling via the transport term, and the kinetic stress boundary condition, introduces nonlocal effects in the stress profile for relatively large stopping distance $\sqrt{v_p v_p}\tau_p$. For large Stokes numbers, these effects can be appreciable and we may expect significant deviations from the local eddy diffusivity (or the characteristic eddy diffusivity). There are, however, clear differences between the density profiles from the kinetic model and the data for all cases. In this respect, we will discuss the role of secondary flow below.

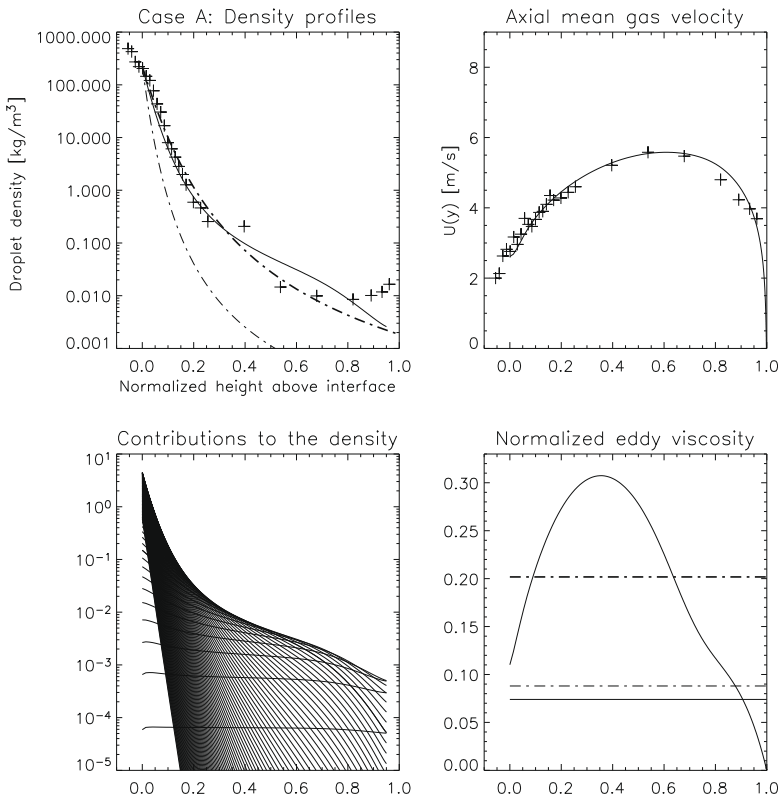

Fig. 2. Case A. The upper left panel shows the density data (crosses) together with the results from the kinetic model (thin full line). The thin dotted line is the result from using the characteristic diffusivity (38), and the thick dash-dotted line is the result from using the cross sectional average scalar diffusivity (40). The lower left panel shows the density profile for all the size bins, as they are calculated from the kinetic theory. Deviations from straight lines are due to turbulence inhomogeneity. The smaller droplets have almost flat profiles, while the large droplets have steep profiles. The upper right panel shows the axial velocity profile together with the data, after tuning R and the interfacial eddy viscosity. The lower right panel shows the eddy diffusivity (or eddy viscosity) normalized to $(h/2)u^*$. The thin horizontal line shows the pipe core value $\zeta = 0.075$, and the thin dotted line shows the diffusivity (38). The thick dotted line shows the average (40).

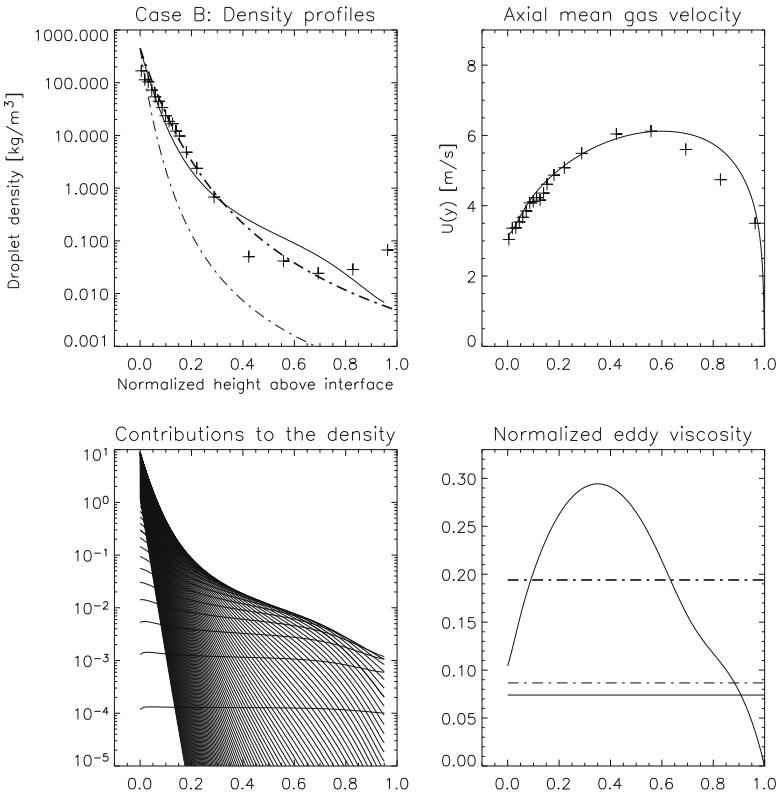

Fig. 3. Case B. The coding is the same as for case A.

The lower left panels (Figs. 2–5) show the density profile for all the size bins, as they are calculated from the kinetic theory. The smaller droplets contribute with almost flat profiles. The large droplets have steep profiles and contribute only near the interface. Only the smaller droplets contribute near the pipe wall. The effect of inhomogeneous turbulence is seen for most of the density

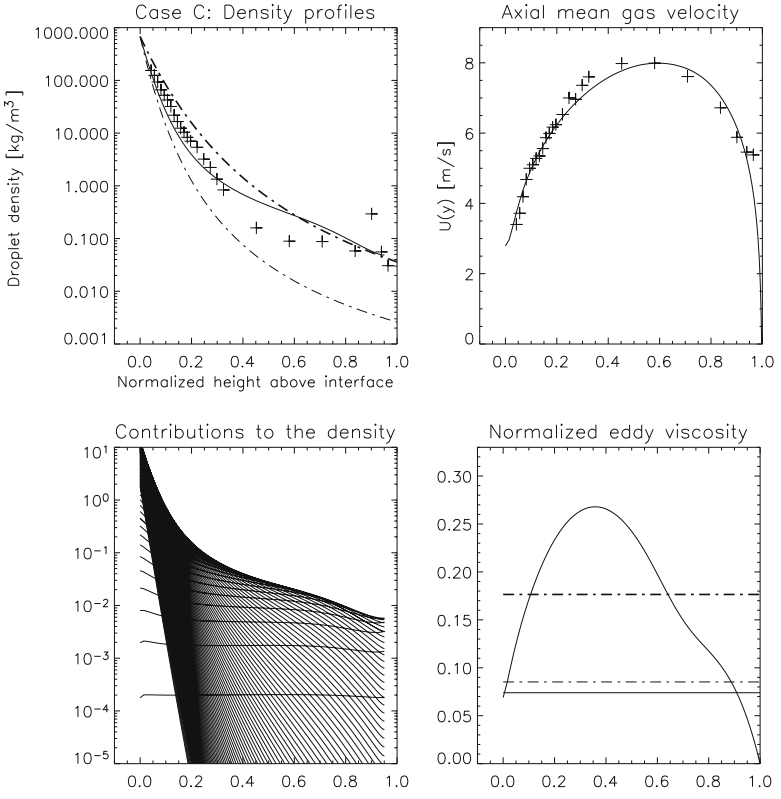

Fig. 4. Case C. The coding is the same as for case A.

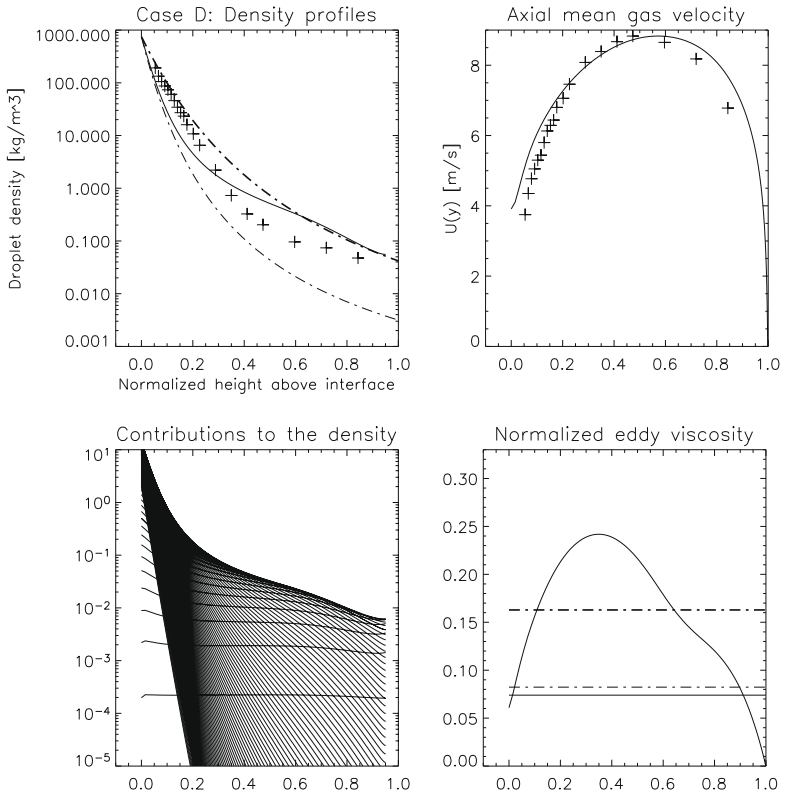

Fig. 5. Case D. The coding is the same as for case A.

profiles (most of the sizes) noting that homogeneous turbulence would have produced linear profiles on the log-plot. A characteristic "bump" is seen in the profiles between 0.6 and 0.8 channel heights, which is due a varying particle diffusivity and the turbophoretic effect that accumulates the droplets where the turbulent kinetic energy is a minimum.

The upper right panels show the axial velocity profile together with the data, after tuning R and the interfacial eddy viscosity.

5.4. Diffusivity and turbophoresis

The momentum equation (15) can be rewritten as the diffusion equation

$$-\epsilon_{yy}\partial_y\rho - \rho\tau_p\partial_y(\overline{v_p v_p}) - \tau_p\rho g_e = 0, \tag{41}$$

where $-\epsilon_{yy}\partial_y\rho$ is the turbulent diffusive mass flux density, $-\rho\tau_p\partial_y(\overline{v_p v_p})$ is the turbophoretic flux, and $-\rho\tau_p g_e$ the gravitational flux. Figs. 6–8 show the corresponding drift velocities obtained by dividing each term by the density (lower left panels). Each figure shows the contributions for a single droplet size for case A. The diffusive and turbophoretic contributions are comparable for the smaller size range, while the diffusive contribution is relatively larger for $d/\bar{d} > 0.1$. Turbophoresis and varying diffusivity influence the concentration profile and its deviation from the leading order exponential, resulting in a characteristic elevated density ("bump") near $y/h \simeq 0.7$ (lower right panels).

The diffusivity is dominated by the inertial term $\tau_p(\overline{v_p v_p})$ for $d/\bar{d} \geqslant 0.4$ (upper right panels), while for the smaller droplets, the fluid induced part $\tau_p\bar{\lambda}_{yy}$ dominates. The limiting value of $\tau_p\bar{\lambda}_{yy}$ is the eddy diffusivity for vanishing size or relaxation time.

The normal stress $\overline{v_p v_p}$ (thick full line in the upper left panel) is very close to the local value $\tau_p\bar{\mu}_{yy}$ (thin full line) obtained by ignoring the Chapman–Enskog transport term in the stress equation. The lower boundary value of the kinetic stress is set close to the local value, such that also for the more inertial particles, the local and non-local stress values are comparable.

The total particle diffusivity (thick full line, upper right panels) tends to be significantly less than the eddy diffusivity (thin full line) in the lower half of the flow volume for the larger droplets ($d/\bar{d} > 1.0$ in Fig. 8). The reason for this is the smoothing effect of the Chapman–Enskog transport term in the kinetic stress equation. The concentration profile is therefore steeper closer to the interface where the larger particles dominate.

5.5. Effects of secondary flow

The basic source of secondary flow in a general sense is anisotropy of the normal stresses in a plane perpendicular to the mean flow (Speziale, 1982). Previous experimental work (e.g., Williams et al., 1996) and simulation work (e.g., van't Westende et al., 2007), clearly suggest that secondary flow can be significant in a pipe cross section. Reynolds stress anisotropy in pipe flow can be induced by several different mechanisms such as varying roughness of the liquid film along the wall perimeter, non-circular cross section of the gas volume (Speziale, 1982), droplet concentration gradients and finally waves on the gas–liquid interface (Nordsveen and Berthelsen, 1997). The two more robust mechanisms in pipe flow is probably the wall roughness effect and the non-circular cross section effect, since these are present regardless of the existence of well defined interfacial waves and details in the concentration profile.

To leading order, the secondary flow pattern is symmetric with respect to the vertical centerline in a pipe. The most simple flow configuration is two counter-rotating, axially aligned vortices (van't Westende et al., 2007) resulting in the circulation shown in Fig. 9, with downflow along the vertical centerline. The LES-simulation of van't Westende et al. (2007) includes the wall roughness

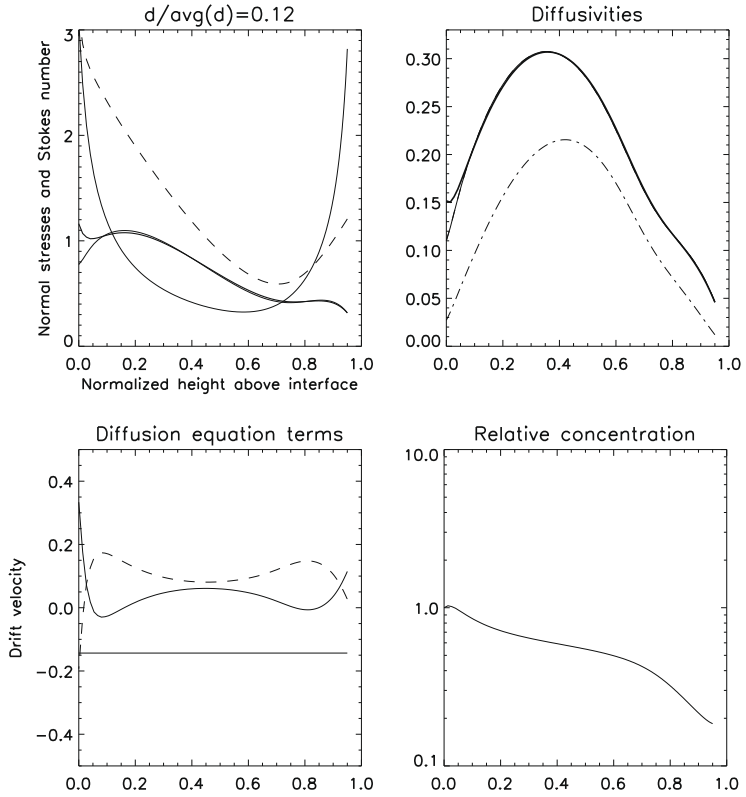

Fig. 6. Diffusivity and turbophoresis for the droplet size $d/\bar{d} = 0.12$. The upper left panel shows the Stokes number $\tau_p/\tau(y)$ (thin, U-shaped line), particle normal stress (thick full line), local estimate of the particle normal stress (thin, full line) and the fluid normal stress (dashed line). The upper right panel shows the total diffusivity $\tau_p(\overline{v'v'} + \bar{\lambda}_{yy})$ (thick line), the fluid contribution $\tau_p\bar{\lambda}_{yy}$ (dashed line) and the eddy viscosity (thin full line). The lower left panel shows the diffusion equation terms normalized by density. The dashed line shows the diffusion velocity $-\epsilon_{yy}\partial_y \ln(\rho)$, the thin full line shows the turbophoretic velocity $-\tau_p\partial_y(\overline{v_p'v_p'})$, and the thin straight line shows the gravitational velocity (settling velocity) $\tau_p g_e$. The lower right panel shows the relative concentration.

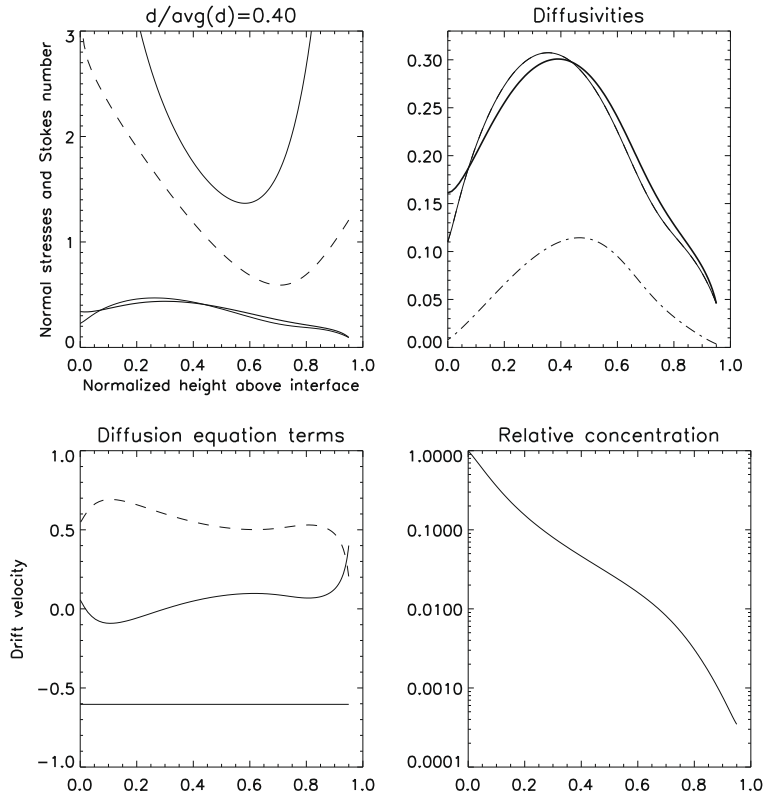

Fig. 7. Diffusivity and turbophoresis for the droplet size $d/\bar{d} = 0.4$. The coding is the same as for Fig. 6.

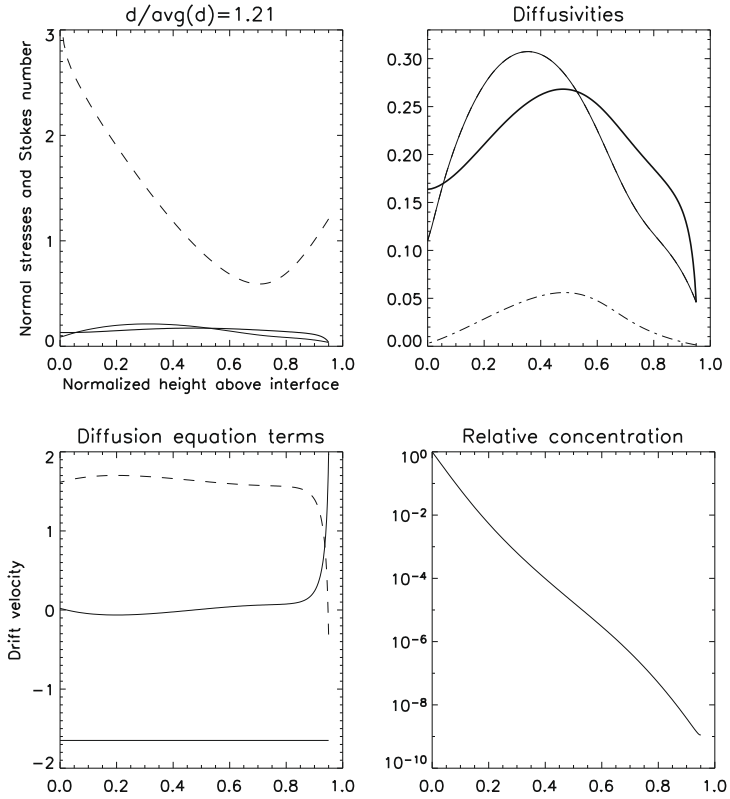

Fig. 8. Diffusivity and turbophoresis for the droplet size $d/\bar{d} = 1.2$. The coding is the same as for Fig. 6. Note the deviation between the total diffusivity $\tau_p(\overline{vv} + \bar{\lambda}_{yy})$ (thick line, upper right panel) and the eddy viscosity (thin full line), due to increasing effect of particle inertia.

effect, and demonstrates an upflow along the pipe walls opposite the roughness gradient of the wall film, and a downflow along the vertical diameter. The magnitude of the secondary flow was about 1–2% of the maximum axial flow velocity.

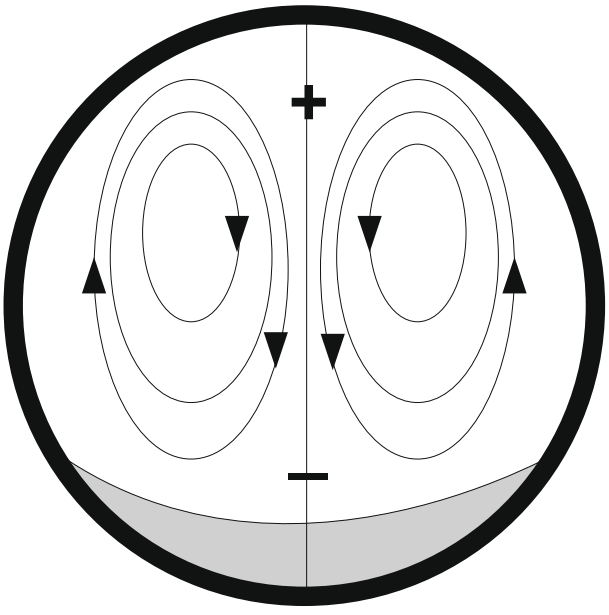

Fig. 9. Qualitative secondary flow streamlines based on the variation of the liquid film roughness and non-circular gas flow cross section. We assume two counter-rotating axial vortices as indicated. The pattern is symmetric with respect to the vertical centerline, and the flow is purely vertical and downwards along this line. '+' indicates a region with converging mass flux giving an excess density for a passive tracer. '−' indicates a region of mass flux divergence. The grey shaded area in the bottom of the pipe illustrates the liquid layer.

The response of the droplets to the secondary flow depends on the Stokes number. Inertial particles will be quite insensitive to the secondary flow, while smaller droplets behave more as passive tracers, and follow more closely the secondary flow pattern. We will assume that the secondary flow velocity component for the smaller droplets will be equal to the secondary flow component of the fluid, and scale down in magnitude with increasing Stokes number. Therefore, a convergent and compressible secondary gas flow near the top of the pipe will increase the density of the smaller droplets locally.

For simplicity, we assume a "quasi-2D" description along the vertical diameter by including effects of convergent/divergent horizontal flow in the particle equations, and by keeping the channel flow Reynolds stress equations unchanged. We will specify a vertical flow profile corresponding to the pattern in Fig. 9. We note that a substantially more complicated 2D cross sectional description for the kinetic theory, accompanying a Reynolds stress driven mean flow, is needed to model the secondary flow effect in a fully consistent manner.

The vertical component of the particle momentum equation in a Cartesian 2D description is, with w-velocity components in the spanwise (horizontal) direction z,

$$\partial_y\left(\rho\overline{v_p v_p} + \rho V_p^2\right) + \partial_z(\rho\overline{w_p v_p} + \rho W_p V_p) + \rho g_e + \rho\beta(V_p - V) = -\partial_y(\bar{\lambda}_{yy}\rho) - \partial_z(\bar{\lambda}_{zy}\rho) - \bar{\gamma}_y\rho. \quad (42)$$

We may solve this equation along the vertical centerline by specifying the terms that couple to the horizontal direction. Before we proceed, we will assume that ∂_z-gradients in the turbulent shear stress $\rho\overline{w_p v_p}$ and $\rho\bar{\lambda}_{zy}$ can be ignored at the centerline. Using the continuity equation $\nabla\cdot(\rho\mathbf{V}_p) = 0$ for the particles, and $\partial_z V_p = 0$ at the centerline (V_p is the most negative here),

$$\partial_y\left(\rho V_p^2\right) + \partial_z(\rho W_p V_p) = \rho\partial_y\left(V_p^2/2\right). \quad (43)$$

These considerations enable (42) to be solved for ρ, with a given mean vertical velocity V_p,

$$\rho\partial_y(V_p^2/2)+\partial_y\left(\rho\overline{v_p v_p}\right)+\rho g_e+\rho\beta(V_p-V)=-\partial_y\left(\bar{\lambda}_{yy}\rho\right)-\bar{\gamma}_y\rho. \tag{44}$$

The formal solution of (44) then assumes the previous exponential form,

$$\rho(y)=\rho(0)\frac{\epsilon_{yy}(0)}{\epsilon_{yy}(y)}\exp\left\{-\tau_p\int_0^y\frac{g_e+\bar{\gamma}_y+\left[\beta(V_p-V)+\partial_y\left(V_p^2/2\right)\right]}{\epsilon_{yy}}d\zeta\right\}. \tag{45}$$

The effect of secondary flow in the kinetic stress will be ignored, keeping the stress equation on the form (16).

When $(V_p-V)>0$ (gas downflow relative to the mean particle velocity at the centerline), the background fluid provides a downward frictional force, adding onto the effect of gravity. This reduces the local scale height and steepens the density gradient. The "dynamic pressure" term $\partial_y\left(V_p^2/2\right)$ represents the effect of the converging/diverging secondary flow along the centerline. For the upper half of the pipe, this term is positive and the flow convergence elevates the density (the effect is opposite in the lower half of the pipe where the flow diverges).

The secondary flow along the centerline due to a single vortex pair is fitted by the smooth function

$$V=-\xi(y), \tag{46}$$

with $\xi>0$. For small droplets we will require $(V_p-V)\to 0$ although we do not formally account for true passive tracers within the regime of the adopted equation of motion (requiring that the particle/fluid density ratio is large). A suitable model for the mean particle velocity may then be defined by

$$V_p=\frac{V}{1+\chi g\tau_p/u^*} \tag{47}$$

giving the following drag force per unit mass due to secondary flow,

$$\beta(V_p-V)=\frac{\chi g}{1+\chi g\tau_p/u^*}\frac{\xi(y)}{u^*}. \tag{48}$$

Here, χ is a tunable factor. We find that $\chi=0.1$ gives a reasonable fit to the concentration profile, and this choice makes the drag force contribution smaller than $\partial_y(V_p^2/2)$ in (45).

Figs. 10 and 11 for cases A and C show the best fit density profiles when a secondary flow profile on the form

$$V(y)=M(y/h-1)\exp^{(y/h-1)/H_s}+N \tag{49}$$

is applied (cases B and D show similar results). For all cases, the imposed secondary flow gives a significant effect in the concentration profiles in the upper half of the flow volume, giving qualitatively correct results. We use the same secondary flow velocity profile for a given axial superficial velocity, and assume that the secondary flow velocity does not depend on the gas density.

The adopted velocity profile is qualitatively similar to that of van't Westende et al. (2007), with the extremal value located near $y/h\simeq 0.7$. The lower right panels show the assumed secondary flow velocity normalized to the wall friction velocity. The maximum velocities correspond to about 0.35 m/s for cases A (and B), and 0.25 m/s for cases C and D. This is comparable to the LES-values of van't Westende.

We may also construct a first order density profile corrected for secondary flow, by adopting constant value ϵ for the diffusivity, and $\bar{\gamma}_y=0$ as discussed earlier. Eq. (45) then reduces to

$$\rho(y)=\rho(0)\exp\left\{\frac{-\tau_p g_e}{\epsilon}y\right\}\exp\left\{-\frac{\tau_p}{\epsilon}\int_0^y\left[\beta(V_p-V)+\partial_y\left(V_p^2/2\right)\right]d\zeta\right\}, \tag{50}$$

where the last exponential term represents a correction to the first order profile. This approach can be justified since the smaller drop-

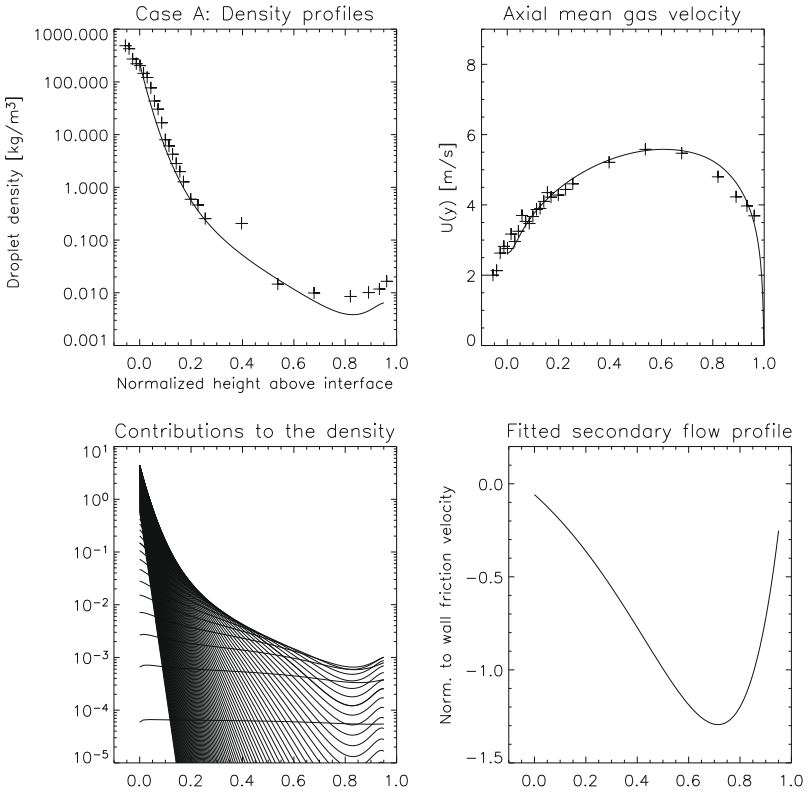

Fig. 10. Case A with secondary flow. The upper left panel shows the density data (crosses) together with the results from the kinetic model including secondary flow (thin full line). The lower left panel shows the density profile for all the size bins. The upper right panel shows the axial velocity profile together with the data, which is assumed to be unaffected by the secondary flow. The lower right panel shows the assumed secondary flow velocity V along the vertical centerline.

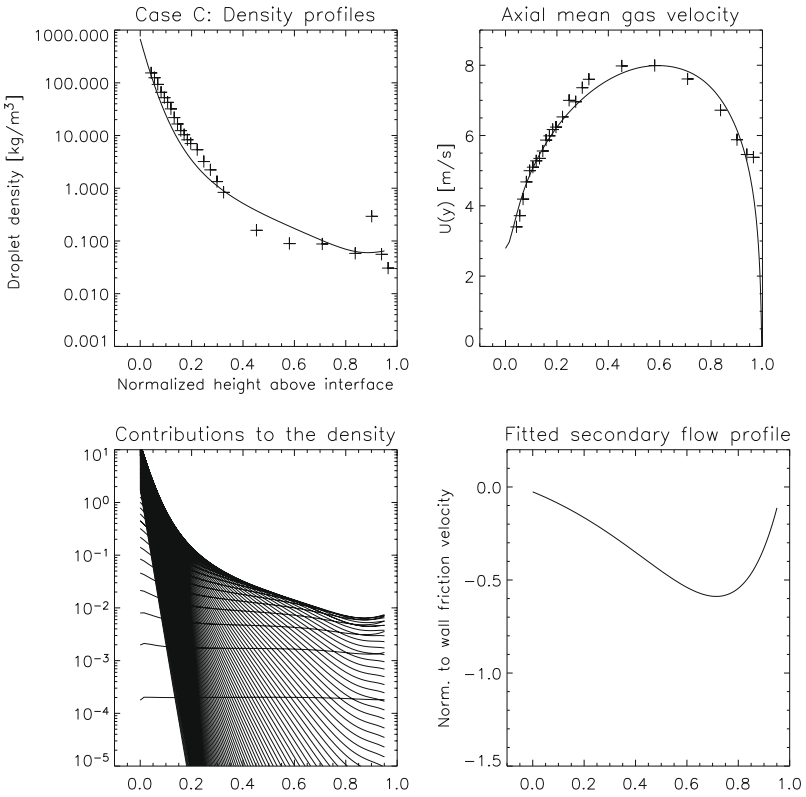

Fig. 11. Case C with secondary flow. The coding is the same as for Case A with secondary flow.

lets dominate at large height where the secondary velocity has the largest impact. Thus, one can choose a local value of the eddy diffusivity (for large heights) and use (50) for the smaller droplets, as an improved first order solution.

6. Summary and conclusions

6.1. Model properties

A model for the droplet concentration profile in turbulent gas–liquid flow in horizontal channels has been developed. The novelty of the current approach is the combination of the kinetic theory of Reeks (1992) to describe the droplets in each size bin, with the Reynolds stress model of Wilcox (2006) for the gas turbulence. We assume a Rosin–Rammler size distribution, and neglect coalescence and breakup in the gas flow, and wall deposition effects on the concentration. We have neglected the back reaction on the gas turbulence (two-way coupling is ignored). An entrainment correlation due to Schadel and Hanratty (1989) is used to describe the boundary concentration near the large scale gas–liquid interface.

The model is compared to measured concentration profiles and velocity profiles along the vertical diameter in the pipe cross section for four different combinations of gas velocity (in the range 6–7 m/s) and gas density (in the range 20–30 kg/m^3). The data are taken from Tayebi et al. (2000), using SF_6 gas and Exxsol oil in a 10 cm diameter horizontal pipe. These experiments utilised an iso-kinetic probe.

The strength of the kinetic theory lies in the fact that it predicts a generalized particle diffusivity valid for all Stokes numbers (or droplet sizes), such that both the "passive tracer regime" of the smaller droplets, and the "free flight regime" of the larger droplets, can be included in the same consistent description. The latter population of droplets is subject to a diffusivity which is (1) non-local and (2) sensitive to the fluctuation kinetic energy at the large scale interface. Furthermore, the theory accounts for turbophoresis, which is migration of particles (droplets) away from regions of large particle kinetic energy.

6.2. Modelling results

We find that varying diffusivity and turbophoresis accumulate droplets near the core region of the flow, where the turbulent kinetic energy of the gas is at a minimum. The concentration profile in the upper half of the flow volume is due to the smaller droplets, which are subject to a diffusivity that is close to the eddy diffusivity. In the low velocity cases (A and B) the measured droplet concentration is *increasing* towards the upper pipe wall (concentration inversion). We demonstrate that when a compressible double-vortex secondary flow is included in the model, we obtain excellent agreement to the data in all cases. van't Westende et al. (2007) shows via LES simulations that the smaller droplets advect into a stagnation point between the vortices, leading to increased droplet density near the upper pipe wall. Accumulation of droplets near the upper wall is of importance in the context of wall deposition of corrosion inhibitor that may be carried by the droplets.

The concentration near the large scale gas/fluid interface is dominated by the larger droplets. The corresponding diffusivity may deviate significantly from the eddy diffusivity, and we find a lower local diffusivity near the interface. This leads to a steeper concentration than what would result if we applied the eddy diffusivity. A reliable prediction of the concentration profile near the interface is important for estimating the mass flux or transport rate of droplets in the gas flow, since the largest flux contribution will be found near the interface where the concentration is large, and the gas velocity is large.

A simplified "first order model" that adopts a single characteristic particle diffusivity, gives reasonable order of magnitude estimates of the droplet concentration, provided that the cross

sectionally averaged eddy diffusivity from the full turbulence model is adopted. This diffusivity is larger than the classical pipe core value which is often used in droplet transport modelling (e.g., Paras and Karabelas, 1991 for air–water flow). The above-mentioned effects in the concentration profile (modified diffusivity for large droplets and secondary flow effects for small droplets) will not be captured by first order modelling. This may lead to an overestimated average droplet transport rate (due to the larger droplets), or an underestimated droplet concentration near the top of the pipe (due to the smaller droplets).

The applicability of the complete model is straightforward, since only tridiagonal matrix equations need to be solved. These equations are nonlinear and iterations are needed to solve them. A number of auxiliary variables are available from the turbulence model, such as the axial velocity profile. Hence, the axial droplet flux may be calculated. We note that a full wall-to-wall cross sectional model is not treated in this work. Such an effort requires a self-consistent treatment of the turbulence across the large scale gas/liquid interface.

6.3. Considerations on the scaling of the concentration profile with respect to pipe diameter

We compared the model to experimental data from a 10*cm* diameter pipe. Oil/gas field conditions correspond to much larger diameters (a factor of 10 larger), and it is thus of interest to examine the scaling property of the concentration profiles, with respect to pipe diameter.

In the context of first order modelling, the scaling of the concentration profile with respect to the flow volume height h (or pipe radius with given holdup) depends on (a) the characteristic scale height H_i, which is the ratio between the characteristic particle diffusivity and the settling velocity of a droplet of diameter $d_i, H_i = \epsilon(d_i)/[g\tau_p(d_i)]$, and (b) the concentration boundary condition. The scaling properties of the diffusivity for large and small droplets are different (as demonstrated using the kinetic theory). For the larger droplets, the particle kinetic stress dominates and non-local transport of kinetic stress may be important (in the limiting case, the droplet trajectories are close to ballistic and the carrier phase plays only a minor role).

For the smaller droplets, local turbulent diffusion is the important effect, and the characteristic diffusivity scale as $\epsilon \sim hu^*_{\mathrm{eff}}$, where u^*_{eff} is a characteristic friction velocity (characteristic turbulent velocity) and h is the flow volume height (see the diffusivities defined by Eqs. (38) and (40)). The dimensionless scale height for a given particle size d_i, will then scale as $H_i/h \sim u^*_{\mathrm{eff}}/g\tau_p(d_i)$. That is, for small droplets, the scale height is proportional to the flow volume height h provided that the left-hand side of the equation (or u^*_{eff}) is kept constant.

The droplet size distribution is likely to vary with h, since the mean droplet size and size variance depends on the gas turbulence level at the interface and in the gas volume. Entrainment (atomization) and deposition rates also depend on the turbulence level at the interface. Future analysis is necessary to clarify how the boundary condition and the droplet size distribution depend on h. This is to some extent dependent on more fundamental research on the turbulent gas/liquid interface, and droplet breakup in turbulent gas. Advanced numerical CFD and experimental work, together with physical modelling, are strongly encouraged to gain more insight in the scaling properties.

Acknowledgements

This work has been funded by the Research Council of Norway via "Strategic Institute Project ES132014, Droplet Transport Modeling and Generation Enhancement in Hydrocarbon Multiphase transport". M.W. Reeks, D.C. Swailes and P. van Dijk of the University of Newcastle, UK, are thanked for valuable discussions.

Appendix A. Supplementary data

Supplementary data associated with this article can be found, in the online version, at doi:10.1016/j.ijmultiphaseflow.2009.03.009.

References

Azzopardi, B.J., 1985. Drop sizes in annular two-phase flow. Exp. Fluids 3, 53.
Berthelsen, P.A., Ytrehus, T., 2005. Calculations of stratified wavy two-phase flow in pipes. Int. J. Multiphase Flow 31, 571.
Biberg, D., 2005. Mathematical models for two-phase stratified pipe flow, Ph.D. Thesis, University of Oslo.
Binder, J.L., Hanratty, T.J., 1992. Use of Lagrangian methods to describe drop deposition and distribution in horizontal gas–liquid annular flows. Int. J. Multiphase Flow 18, 803.
Crowe, C.T., 2000. On models for turbulence modulation in fluid–particle flows. Int. J. Multiphase Flow 26, 719.
Drazen, D., Jensen, A., 2007. Time-resolved combined PIV/PTV measurements of two-phase turbulent pipe flow. In: Proceedings of the Sixth International Conference on Multiphase Flow, ICMF 2007, Leipzig, Germany, July 9–13, 2007.
Durbin, P.A., Medic, G., Seo, J.-M., Eaton, J.K., Song, S., 2001. Rough wall modification of two-layer k–ϵ. J. Fluids Eng., Trans. ASME 123, 16.
Guha, A., 1997. A unified Eulerian theory of turbulent deposition to smooth and rough surfaces. J. Aerosol Sci. 28, 1517.
Hyland, K.E., McKee, S., Reeks, M.W., 1999. Derivation of a pdf kinetic equation for the transport of particles in turbulent flows. J. Phys. A 32, 6169.
McCoy, D.D., Hanratty, T.J., 1977. Rate of deposition of droplets in annular two-phase flow. Int. J. Multiphase Flow 3, 319.
Newton, C.H., Behnia, M., 2001. A numerical model of stratified wavy gas–liquid pipe flow. Chem. Eng. Sci. 56, 6851.
Nordsveen, M., Berthelsen, A.F., 1997. Wave induced secondary motions in stratified duct flow. Int. J. Multiphase Flow 23, 503.
Paras, S.V., Karabelas, A.J., 1991. Droplet entrainment and deposition in horizontal annular flow. Int. J. Multiphase Flow 17, 455.
Reeks, M.W., 1992. On the continuum equations for dispersed particles in nonuniform flows. Phys. Fluids A 4, 1290.
Reeks, M.W., 2001. Particle drift in turbulent flows: the influence from local structure and inhomogeneity. In: ICMF 2001, New Orleans, 2001, No. 187.
Reeks, M.W., 2005. On model equations for particle dispersion in inhomogeneous turbulence. Int. J. Multiphase Flow 31, 93.
Rivkind, V.Y., Ryskin, G.M., 1976. Flow structure in motion of a spherical drop in a fluid medium at intermediate Reynolds number. Fluid Dyn. (USSR) 11, 5.
Schadel, S.A., Hanratty, T.J., 1989. Interpretation of atomization rates of the liquid film in gas–liquid annular flow. Int. J. Multiphase Flow 15, 893.
Sergeev, Y.A., Johnson, R.S., Swailes, D.C., 2002. Dilute suspension of high inertia particles in the turbulent flow near the wall. Phys. Fluids 14, 1042.
Skartlien, R., 2006. First order model for droplet transport in stratified gas flow. IFE-Report, IFE/KR/F-2006/110.
Skartlien, R., 2007. Kinetic modeling of particles in stratified flow – evaluation of dispersion tensors in inhomogeneous turbulence. Int. J. Multiphase Flow 33, 1006.
Skartlien, R., 2007b. Evaluation of a kinetic theory model for inertial particles in stratified turbulent flow – the influence of the Stokes number. In: Proceedings of the International Conference on Multiphase Flow, ICMF 2007, Leipzig, Germany, July 9–13, 2007.
Speziale, C.G., 1982. On turbulent secondary flows in pipes of non-circular cross-section. Int. J. Eng. Sci. 20, 863.
Swailes, D.C., Sergeev, Y.A., Parker, A., 1998. Chapman–Enskog closure approximation in the kinetic theory of dilute turbulent gas-particulate suspensions. Physica A 254, 517.
Tatterson, D.F., 1975. Rate of atomization and drop size in annular two-phase flow, Ph.D. Thesis, University of Illinois, Urbana, USA.
Tayebi, D., Nuland, S., Fuchs, P., 2000. Droplet transport in oil/gas and water/gas flow at high gas densities. Int. J. Multiphase Flow 26, 741.
Ueda, T., 1979. Entrainment rate and size of entrained droplets. Bull. JSME 22, 171.
van't Westende, J.M.C., Belt, R.J., Portela, L.M., Mudde, R.F., Oliemans, R.V.A., 2007. Effect of secondary flow on droplet distribution and deposition in horizontal annular pipe flow. Int. J. Multiphase Flow 33, 67.
Wilcox, C.D., 2006. Turbulence Modelling for CFD, second ed. DCW Industries.
Williams, L.R., Dykhno, L.A., Hanratty, T.J., 1996. Droplet flux distributions and entrainment in horizontal gas–liquid flows. Int. J. Multiphase Flow 22, 1.
Yoon, S.S., 2005. Droplet distributions at the liquid core of a turbulent spray. Phys. Fluids 17, 035101–035103.
Young, G., Leeming, A., 1997. A theory of particle deposition in turbulent pipe flow. J. Fluid Mech. 340, 129.
Zaichik, L.I., Alichenkov, V.M., 2005. Statistical models for predicting particle dispersion and preferential concentration in turbulent flows. Int. J. Heat Fluid Flow 26, 416.